

Cite this: *Chem. Sci.*, 2024, 15, 9173

All publication charges for this article have been paid for by the Royal Society of Chemistry

# Restructuring multi-phase interfaces from Cu-based metal–organic frameworks for selective electroreduction of CO<sub>2</sub> to C<sub>2</sub>H<sub>4</sub>†

Jiye Feng,<sup>a</sup> Wenbiao Zhang,<sup>ab</sup> Danni Shi,<sup>a</sup> Yingshuai Jia,<sup>b</sup> Yi Tang,<sup>b</sup> Yuying Meng<sup>b</sup> and Qingsheng Gao<sup>\*,a</sup>

Multi-phase interfaces are promising for surmounting the energy barriers of electrochemical CO<sub>2</sub> reduction involving multiple electron transfer steps, but challenges still remain in constructing interfacial microstructures and unraveling their dynamic changes and working mechanism. Herein, highly active Ag/Cu/Cu<sub>2</sub>O heterostructures are *in situ* electrochemically restructured from Ag-incorporating HKUST-1, a Cu-based metal–organic framework (MOF), and accomplish efficient CO<sub>2</sub>-to-C<sub>2</sub>H<sub>4</sub> conversion with a high faradaic efficiency (57.2% at –1.3 V vs. RHE) and satisfactory stability in flow cells, performing among the best of recently reported MOFs and their derivatives. The combination of *in/ex situ* characterizations and theoretical calculations reveals that Ag plays a crucial role in stabilizing Cu(I) and increasing the CO surface coverage, while the active Cu/Cu<sub>2</sub>O interfaces significantly reduce the energy barrier of C–C coupling toward the boosted ethylene production. This work not only proves MOFs as feasible precursors to derive efficient electrocatalysts on site, but also provides in-depth understanding on the working interfaces at an atomic level.

Received 9th February 2024

Accepted 13th May 2024

DOI: 10.1039/d4sc00967c

rsc.li/chemical-science

## Introduction

The electrochemical CO<sub>2</sub> reduction reaction (CO<sub>2</sub>RR) powered by renewable electricity provides a sustainable process toward carbon neutrality.<sup>1,2</sup> Compared with C<sub>1</sub> products (*e.g.*, CO, HCOOH, and CH<sub>4</sub>), C<sub>2+</sub> ones (*e.g.*, C<sub>2</sub>H<sub>4</sub> and C<sub>2</sub>H<sub>5</sub>OH) feature higher energy density and market value; however, their productivity is seriously limited by the multi-step hydrogenation competing with a series of side-reactions.<sup>3–5</sup> So far, Cu is the only metal that can selectively convert CO<sub>2</sub> to C<sub>2+</sub> thanks to the benign bonding of \*CO intermediates,<sup>6,7</sup> and its interfaces with tailored valence states, grain boundaries and unsaturated sites are evidenced to surmount the energy barriers of such multiple electron transfer steps.<sup>8–10</sup> Although progress has been made in C<sub>2+</sub> production, it's still challenging to facilely construct active interfaces and effectively stabilize them during electrolysis.<sup>11</sup>

Metal–organic frameworks (MOFs) have attracted extensive interest for the electrochemical CO<sub>2</sub>RR associated with the high

surface area, controllable pore size/shape, and open metal sites,<sup>12–14</sup> but as for the catalytic mechanism debates remain due to the dynamic change of frameworks during the tough electrolysis.<sup>15</sup> In particular, Cu-based MOFs containing frangible Cu–O<sub>4</sub> nodes would undergo *in situ* reconstruction since the electron transport along networks *via* the copper-ion redox demolishes the coordination extensively.<sup>16</sup> The newly formed surface/interfaces, rather than the initial frameworks, should be brought into sharp focus for the mechanism study.<sup>17</sup> Following the progressive insights, such electrochemical reconstruction was proved feasible to produce active and selective catalysts on site,<sup>18–22</sup> avoiding the time and energy-consuming preparation of catalysts and working electrodes (*e.g.*, thermally driven epitaxial growth of multi-phase interfaces<sup>23,24</sup> and ultrasonic spraying for loading powdery electrocatalysts onto gas-diffusion electrodes<sup>25</sup>). The *in situ* derived electrocatalysts inherit the structural merits of MOFs, and more importantly generate plenteous interfaces abundant with coordinatively unsaturated sites under the manipulated electrochemical conditions.<sup>26</sup> For example, the single-type Cu<sub>2</sub>O sites of Cu<sub>2</sub>O@CuHHTP and coordinatively unsaturated Cu paddle wheel clusters (Cu<sub>2</sub>(–HCOO)<sub>3</sub>), partially reduced from CuHHTP and HKUST-1 at mild potentials, promoted the selective CO<sub>2</sub>RR to CH<sub>4</sub> in H-type reactors, while C<sub>2+</sub> production was still restricted.<sup>17,19</sup> Moreover, the structure–activity relationship under working conditions was inconclusive in the context of the further reconfiguration at more negative potentials and higher current densities adopted for the CO<sub>2</sub>RR, especially in flow cells. As

<sup>a</sup>College of Chemistry and Materials Science, Guangdong Provincial Key Laboratory of Functional Supramolecular Coordination Materials and Applications, Jinan University, Guangzhou 510632, P. R. China. E-mail: tqsgao@jnu.edu.cn

<sup>b</sup>Department of Chemistry, Shanghai Key Laboratory of Molecular Catalysis and Innovative Materials, Laboratory of Advanced Materials, Collaborative Innovation Centre of Chemistry for Energy Materials, Fudan University, Shanghai 200433, P. R. China

† Electronic supplementary information (ESI) available: Additional figures and data for CO<sub>2</sub>RR performance, EDS mapping, additional XRD, IR, XPS and CVs, NMR spectra, XANES and EXAFS. See DOI: <https://doi.org/10.1039/d4sc00967c>

recently highlighted, the deep reconstruction of sulfur-doped HKUST-1 to ligand-free Cu/Cu<sub>x</sub>S<sub>y</sub> interfaces could enable efficient ethylene production;<sup>18</sup> however, such effort was hampered by the difficult control over the exchange of benzenetricarboxylic linkers by thioacetamide ligands in frangible frameworks. In other words, constructing, promoting and stabilizing interfacial active species, *e.g.*, Cu(0)–Cu(I) ensembles and defective sites, *via* elaborative MOF reconstruction are promising for robust C<sub>2</sub>+ production, but still an arduous task under the harsh CO<sub>2</sub>RR conditions.<sup>27,28</sup>

Thanks to the thermodynamic merits of Ag in comparison with Cu, *e.g.*, the relatively higher standard redox potential ( $E_{\text{Ag}^+/\text{Ag}} = +0.80 \text{ V vs. } E_{\text{Cu}^+/\text{Cu}} = +0.52 \text{ V}$ ) and the less negative formation enthalpy of oxides ( $-31.1 \text{ kJ mol}^{-1} \text{ Ag}_2\text{O vs. } -169 \text{ kJ mol}^{-1} \text{ Cu}_2\text{O}$ ), introducing foreign Ag atoms is anticipated to stabilize neighboring Cu(I) active for the CO<sub>2</sub>RR.<sup>29</sup> Moreover, it's also expected to empower tandem electrolysis on the expanded interfaces *via* available \*CO spillover from weakly bonding Ag to Cu(0)–Cu(I) sites capable of C–C coupling.<sup>30–32</sup> However, the relevant research is still absent for directional MOF reconstruction. Here, Ag-incorporating HKUST-1 frameworks (Ag<sub>*n*</sub>/HKUST-1, *n* denotes the molar ratio of Ag/Cu) were for the first time introduced to *in situ* restructure Ag/Cu/Cu<sub>2</sub>O heterostructures under practical electrolysis conditions, which were highly active for CO<sub>2</sub>-to-C<sub>2</sub>H<sub>4</sub> conversion due to the rich Cu(I) species and Ag/Cu/Cu<sub>2</sub>O interfaces. With an optimal loading of Ag ( $n_{\text{Ag}} : n_{\text{Cu}} = 0.1$ ), the *in situ* derived electrocatalysts afforded a high C<sub>2</sub>H<sub>4</sub> faradaic efficiency (FE) of 57.2% at  $-1.3 \text{ V vs. RHE}$ , superior to those of HKUST-1 derivatives (17.4%), electro-deposited Ag/Cu/Cu<sub>2</sub>O (16.7%), and their recently reported MOF-related counterparts, and maintained satisfactory long-term durability. The combination of *in/ex situ* characterizations and theoretical calculations confirmed that Ag played a crucial role in stabilizing Cu(I) and increasing CO surface coverage, while the resulting rich Cu/Cu<sub>2</sub>O interface significantly reduces the energy barrier of C–C coupling toward boosted ethylene production.

## Experimental section

### Chemicals

Copper(II) nitrate trihydrate (Cu(NO<sub>3</sub>)<sub>2</sub>·3H<sub>2</sub>O, >99.0%), polyvinylpyrrolidone (PVP, MW 58 000) and *N,N*-dimethylformamide (DMF, 99.8%) were provided by Macklin Co., Ltd (Shanghai, China). 1,3,5-Benzenetricarboxylic acid (H<sub>3</sub>BTC, 98%), potassium hydroxide (KOH, 85%) and silver nitrate (AgNO<sub>3</sub>, 99.8%) were purchased from Aladdin Chemistry Co., Ltd (Shanghai, China). Nafion (5 wt%) solution was purchased from Sigma-Aldrich. Ethanol (99.7%) was bought from Sinopharm Chemical Reagent Co., Ltd. (Shanghai, China). All aqueous solutions were prepared using ultrapure water (>18 MΩ).

### Material synthesis

**Synthesis of HKUST-1.** HKUST-1 was prepared *via* the reported method with a slight modification.<sup>33</sup> Typically, 8.6 mmol of Cu(NO<sub>3</sub>)<sub>2</sub>·3H<sub>2</sub>O was dissolved in 15 mL of deionized water. A

solution of H<sub>3</sub>BTC acid (4.8 mmol) in a co-solvent of DMF and ethanol (30 mL, 1 : 1 by volume) was mixed with 2.0 g of PVP under continuous stirring. After complete dispersion of the reactants, the two solutions were mixed directly. Subsequently, the mixed solution was stirred for 15 min and transferred into a 50 mL Teflon-lined stainless-steel autoclave. The autoclave was heated at 100 °C for 10 h. After naturally cooling down to room temperature, the product was washed with ethanol three times by centrifugation at 8000 rpm for 5 min. Finally, the blue powder of HKUST-1 was obtained after drying under vacuum at 60 °C overnight.

**Synthesis of Ag<sub>*n*</sub>/HKUST-1.** The Ag<sub>0.1</sub>/HKUST-1 pre-catalyst was prepared by a wet chemistry method.<sup>34</sup> 5.4 mg (0.032 mmol) of AgNO<sub>3</sub> was dissolved in 10 mL of hydroalcoholic solution ( $V_{\text{EtOH}} : V_{\text{H}_2\text{O}} = 9 : 1$ ), and then 70 mg (0.32 mmol) of the as-prepared HKUST-1 was added into the above solution with continuous stirring for 20 h at 85 °C. The precipitate was centrifuged, washed with ethanol and dried in a vacuum oven at 60 °C overnight. Furthermore, varied amounts of AgNO<sub>3</sub> were used to prepare Ag<sub>*n*</sub>/HKUST-1 with different amounts of Ag incorporated.

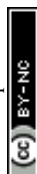
**Synthesis of EtOH reduced HKUST-1 (ER-HKUST-1).** HKUST-1 was added to 10 mL of hydroalcoholic solution ( $V_{\text{EtOH}} : V_{\text{H}_2\text{O}} = 9 : 1$ ) with continuous stirring for 20 h at 85 °C. The precipitate was centrifuged, washed with ethanol and dried in a vacuum oven at 60 °C overnight.

### Physical characterization

Transmission electron microscopy (TEM), energy dispersive spectroscopy (EDS) and the corresponding elemental mapping were performed on a JEOL 2100F. Scanning electron microscopy (SEM) and energy dispersive spectroscopy (EDS) were conducted on a ZEISS ULTRA55. X-ray diffraction (XRD) analysis was performed on a Bruker D8 diffractometer using Cu Kα radiation ( $\lambda = 1.54056 \text{ \AA}$ ). X-ray photoelectron and Auger electron spectroscopies (XPS and AES) were performed on a Thermo Scientific Escalab 250Xi. Fourier transform infrared (FT-IR) spectroscopy was carried out on a PerkinElmer spectrometer with the spectral range of 4000–400 cm<sup>−1</sup>. Raman investigation was performed on a laser confocal Raman microspectrometer (Horiba HR-800) with an excitation laser wavelength of 532 nm. The electron paramagnetic resonance (EPR) spectra were recorded on a Bruker A300. Inductively coupled plasma-optical emission spectrometry (ICP-OES) analysis was conducted on an OPTIMA 2000DV. X-ray absorption spectroscopy (XAS) was performed at beamline 12-BM of the Advanced Photon Source beamline at Argonne National Laboratory in Illinois, USA.

### Preparation of cathode electrodes

5 mg of electrocatalyst was ground to powder and then dispersed into anhydrous ethanol (450 μL) followed by adding 50 μL Nafion. After continuous ultrasonication for at least 30 min, a homogeneous ink was achieved. 100 μL of the ink was pipetted onto a carbon paper electrode (0.5 cm × 2 cm) with a loading of 1 mg cm<sup>−2</sup>. The electrode was then dried at room temperature naturally for the subsequent electrochemical tests.



## Electrochemical test

CO<sub>2</sub> electrolysis was performed in a flow cell. The prepared gas diffusion electrode (GDE) was the working electrode. An electrolyte (1.0 M KOH) was circulated through the flow cell at a rate of 15 mL min<sup>−1</sup> under the pressure applied by a peristaltic pump. Anode and cathode chambers were separated by an anion exchange membrane. A platinum electrode and a solid Ag/AgCl electrode served as the counter electrode and reference electrode, respectively. Electrode potentials in the study were converted to the reversible hydrogen electrode (RHE) scale according to the following equation:

$$E_{(\text{vs. RHE})} = E_{(\text{vs. Ag/AgCl})} + 0.059 \times \text{pH} + 0.197 \text{ V}$$

All electrochemical measurements were carried out in a three-electrode system with a CHI660E potentiostat. Linear sweep voltammetry (LSV) curves were obtained to choose the appropriate potential range for the catalysts. The sweeping range was from 0 to −1.7 V (vs. RHE) at a scan rate of 100 mV s<sup>−1</sup> in 1 M KOH solution with a CO<sub>2</sub> flow.

## Products analysis

Gaseous products were analyzed using a gas chromatograph (GC, FULI-9790 II) equipped with a flame ionization detector (FID for CO and hydrocarbons) and a thermal conductivity detector (TCD for H<sub>2</sub>). Gas-phase products were sampled every 20 min using high-purity nitrogen (N<sub>2</sub>, 99.999%) as the carrier gas. The column effluent (separated gas mixtures) was first passed through the TCD where hydrogen was quantified, then CO, CH<sub>4</sub> and C<sub>2</sub>H<sub>4</sub> were subsequently quantified by the FID. According to the peak areas in the GC, the partial current densities and FEs of CO, CH<sub>4</sub>, C<sub>2</sub>H<sub>4</sub> and H<sub>2</sub> were calculated using the following equations:

$$j_x = \frac{\text{peak area of } x}{\alpha} \times \text{flow rate} \times \frac{nF}{V_m} \times (\text{electrode area})^{-1}$$

$$\text{FE} = \frac{j_x}{j_{\text{total}}}$$

where  $x$  represents one of CO, CH<sub>4</sub>, C<sub>2</sub>H<sub>4</sub> and H<sub>2</sub>, and  $n$  represents the number of electrons to be transferred to form the products, which are 2, 8, 12 and 2, respectively;  $\alpha$  is the conversion factor for CO, CH<sub>4</sub>, C<sub>2</sub>H<sub>4</sub> and H<sub>2</sub>, respectively, based on the calibration of standard samples;  $F$  is the Faraday constant ( $F = 96485 \text{ C mol}^{-1}$ ), and  $V_m = 22.4 \text{ L mol}^{-1}$ .

The liquid products were quantified using <sup>1</sup>H nuclear magnetic resonance (NMR) (AVANCE III HD 400 MHz), in which 0.1 mL of the electrolyte was mixed with 0.5 mL of D<sub>2</sub>O, and DMSO was used as an internal standard.

## Theoretical calculations

DFT calculations were performed at the GGA level within the Perdew–Burke–Ernzerhof (PBE) functional using the CASTEP software implemented in Materials Studio. The total energy

calculation was performed using a kinetic energy cutoff of 450.0 eV assigned to the plane-wave basis set for calculating the density of states. The self-consistent field (SCF) tolerance was  $1 \times 10^{-6}$  eV. The Brillouin zone was sampled using  $5 \times 5 \times 1$   $k$ -points. The core electrons were replaced with ultrasoft pseudopotentials. An fcc Cu model was used to further construct Cu–Ag and Cu–Cu<sub>2</sub>O. The fcc Cu–Ag was constructed by replacing a Cu atom with Ag. Then, we selected a  $3 \times 3$  relaxed rhombus Cu<sub>2</sub>O(001) bilayer on top of a relaxed  $3 \times 3$  Cu(001) surface to model Cu/Cu<sub>2</sub>O heterojunctions, in which O atoms were introduced to saturate the Cu atoms on the Cu(001) thus the surface atoms are well passivated. The Cu(100), Cu–Ag(100) and Cu–Cu<sub>2</sub>O(100) surfaces were modeled using five layer slabs to study the CO<sub>2</sub> reduction activity. A vacuum region of 15 Å between any two repeated slabs was used to avoid interactions between repeated slabs along the  $z$ -direction.

The binding energy (BE) of an adsorbate was calculated as:

$$\text{BE}_{(\text{adsorbate})} = E_{(\text{slab+adsorbate})} - E_{(\text{slab})} - E_{(\text{adsorbate})}$$

where  $E_{(\text{slab+adsorbate})}$ ,  $E_{(\text{slab})}$  and  $E_{(\text{adsorbate})}$  are the total energy of the slab with an adsorbate, the energy of the pure slab/facet and the energy of the adsorbate in the gas phase, respectively.

The Gibbs free energy ( $G$ ) of a species was calculated as:

$$G = E + \text{ZPE} - TS$$

where  $E$  is the total energy of a species obtained from DFT calculations, and ZPE and  $S$  are the zero-point energy and entropy of the species, respectively. A potential of 0 V was adopted in the calculation. The change in free energy ( $\Delta G$ ) was calculated as:

$$\Delta G = \Delta E + \Delta \text{ZPE} - T\Delta S$$

The transition state search used complete LST/QST in 0.25 eV Å<sup>−1</sup> RMS convergence, with the optimized reactant and product geometries as starting points. CASTEP employed algorithms such as the nudged elastic band (NEB) or the dimer method to explore the potential energy surface and locate the transition state structure. The transition state was obtained between reactants and products while minimizing the energy in 10 QST steps.

## Results and discussion

An HKUST-1 framework is built up of dimeric Cu units connected by benzene-1,3,5-tricarboxylate linkers. It was fabricated *via* a previously reported method,<sup>33</sup> and then was incorporated with Ag after reacting with AgNO<sub>3</sub> in a hydroalcoholic solution ( $V_{\text{EtOH}} : V_{\text{H}_2\text{O}} = 9 : 1$ ), where EtOH was the reducing agent that reduced Ag(I) to metallic Ag and partially reduced Cu(II) to Cu(I).<sup>34</sup> Accordingly, we also prepared a reference sample *via* a similar process in the absence of AgNO<sub>3</sub>, which was named EtOH reduced HKUST-1 (ER-HKUST-1).

The crystal structure of the as-prepared samples was analyzed by XRD (Fig. 1a). Ag<sub>0.1</sub>/HKUST-1 presented



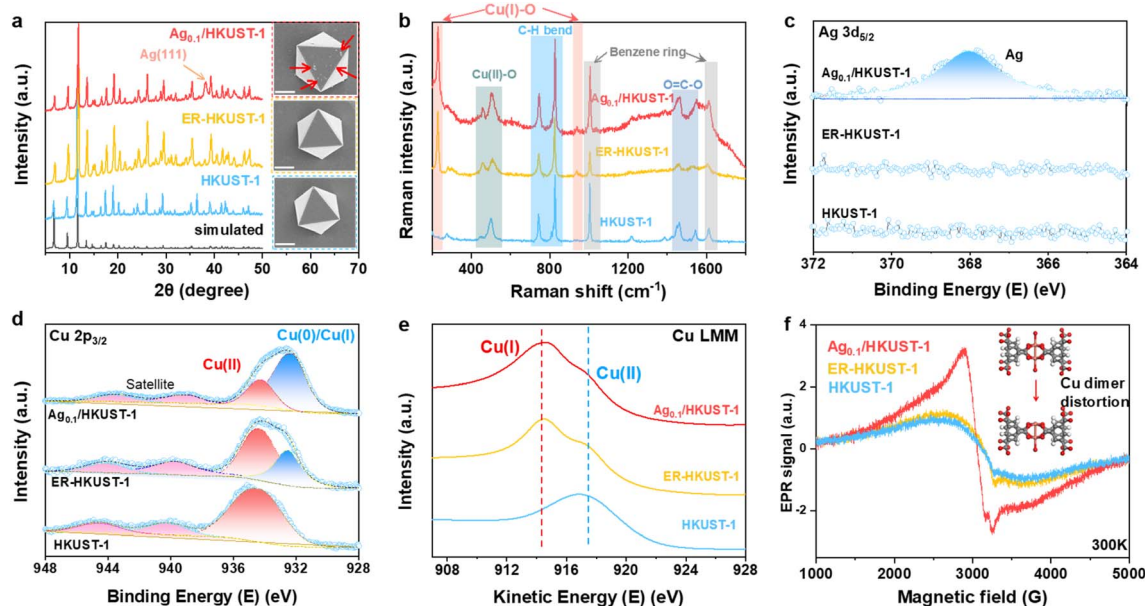


Fig. 1 Structural characterization of HKUST-1, ER-HKUST-1 and Ag<sub>0.1</sub>/HKUST-1: (a) XRD patterns, (insets of a) SEM images with the scale bar of 1 μm, (b) Raman spectra, (c) high-resolution Ag 3d<sub>5/2</sub> XPS, (d) high-resolution Cu 2p<sub>3/2</sub> XPS, (e) Cu LMM AES and (f) EPR spectra.

a characteristic pattern consistent with those of HKUST-1 and ER-HKUST-1, confirming the well-retained framework after Ag loading and partial reduction. This is also supported by their same absorption bands in FT-IR spectra (Fig. S1, ESI†). A new peak of Ag(111) appearing in Ag<sub>0.1</sub>/HKUST-1 indicated the successful loading of Ag. An identical octahedral structure was observed in the three samples by SEM (insets of Fig. 1a), and the small nanoparticles (marked by red arrows) on the surface of Ag<sub>0.1</sub>/HKUST-1 should be assigned to the incorporated Ag. Accordingly, the elemental mapping performed with both SEM and TEM revealed the uniform distribution of O, Cu and Ag elements over Ag<sub>0.1</sub>/HKUST-1 octahedrons (Fig. S2, ESI†). In the Raman spectra (Fig. 1b), two new bands at 218 and 930 cm<sup>-1</sup>, responsible for the Cu(I)-O vibrations,<sup>34</sup> appeared in ER-HKUST-1 and Ag<sub>0.1</sub>/HKUST-1, which indicated the partial reduction of Cu(II) to Cu(I).

The chemical composition and element valence state were further studied by XPS and AES. Different from HKUST-1 and ER-HKUST-1, Ag<sub>0.1</sub>/HKUST-1 displayed a broad Ag 3d peak at 368.1 eV in XPS (Fig. 1c), confirming the successful incorporation of Ag. In the profile of Cu 2p<sub>3/2</sub>, the peak at 934.5 eV was attributed to Cu(II) species, and that at 932.4 eV could be assigned to Cu(0) or Cu(I) (Fig. 1d).<sup>18</sup> AES with the good resolution of Cu(0)/Cu(I) further identified the co-presence of Cu(I) and Cu(II) in both Ag<sub>0.1</sub>/HKUST-1 and ER-HKUST-1, in comparison with the dominant Cu(II) in HKUST-1 (Fig. 1e). Therefore, the peak at 932.4 eV in the Cu 2p<sub>3/2</sub> XPS profile should be ascribed to the Cu(I) species in Ag<sub>0.1</sub>/HKUST-1 and ER-HKUST-1, which was derived from the partial reduction of Cu(II) by EtOH. It's noteworthy that Ag<sub>0.1</sub>/HKUST-1 showed a relatively higher intensity of Cu(I) in both XPS and AES profiles as compared with ER-HKUST-1, suggesting the stabilization of Cu(I) by additive Ag. The presence of Cu(I) would cause the

distortion of the Cu-Cu dimer, as confirmed by the high signal intensity of Ag<sub>0.1</sub>/HKUST-1 in EPR (Fig. 1f).<sup>35</sup> In addition, a series of Ag<sub>n</sub>/HKUST-1 frameworks with an identical structure but different Ag/Cu molar ratios could be obtained after varying the feeding ratio (Fig. S3–S7, ESI†), which showed a volcano relationship between Cu(I)/Cu(II) and Ag/Cu ratios (Fig. S8, ESI†), indicating the enriched Cu(I) at a moderate Ag loading.

We conducted *in situ* Raman analysis combined with a CO<sub>2</sub>RR test at various potentials to assess the reconstruction of such Cu-based MOFs (Fig. S9, ESI†). The bands corresponding to Cu(II)-O and C-H disappeared quickly at the applied bias, indicating the collapse of the metal-organic framework. The emerging band of Cu-CO further suggested the formation of \*CO on the *in situ* formed metallic surface.<sup>36</sup> Of particular interest is the appearance of Cu<sub>2</sub>O bands at 520 and 610 cm<sup>-1</sup> in Ag<sub>0.1</sub>/HKUST-1 and ER-HKUST-1 compared to HKUST-1,<sup>37</sup> whose intensity increased with the negative potentials and reached a maximum at -1.3 V vs. RHE. Thus, the *in situ* reconstruction of the three samples was further analyzed at -1.3 V vs. RHE in a flow cell. As the model sample, Ag<sub>0.1</sub>/HKUST-1 afforded a fluctuating current density initially in chronoamperometry (Fig. 2a), which afterwards became more stable after 1 h electrolysis, suggesting that the reconfiguration can be completed within the first hour. To observe the reconstruction process more directly, the reconstituted samples were subjected to SEM (Fig. 2b–d). Obviously, the octahedral structure collapsed after only 1 min, and the final morphology of HKUST-1 and ER-HKUST-1 was granular, whereas Ag<sub>0.1</sub>/HKUST-1 exhibited dendritic nanostructures that can obviously enhance surface hydrophobicity (Fig. S10, ESI†). As previously evidenced,<sup>38,39</sup> electrocatalysts with a hydrophobic surface would be favorable for the CO<sub>2</sub>RR because of the inhibited hydrogen evolution competition. Interestingly, the reconfigured



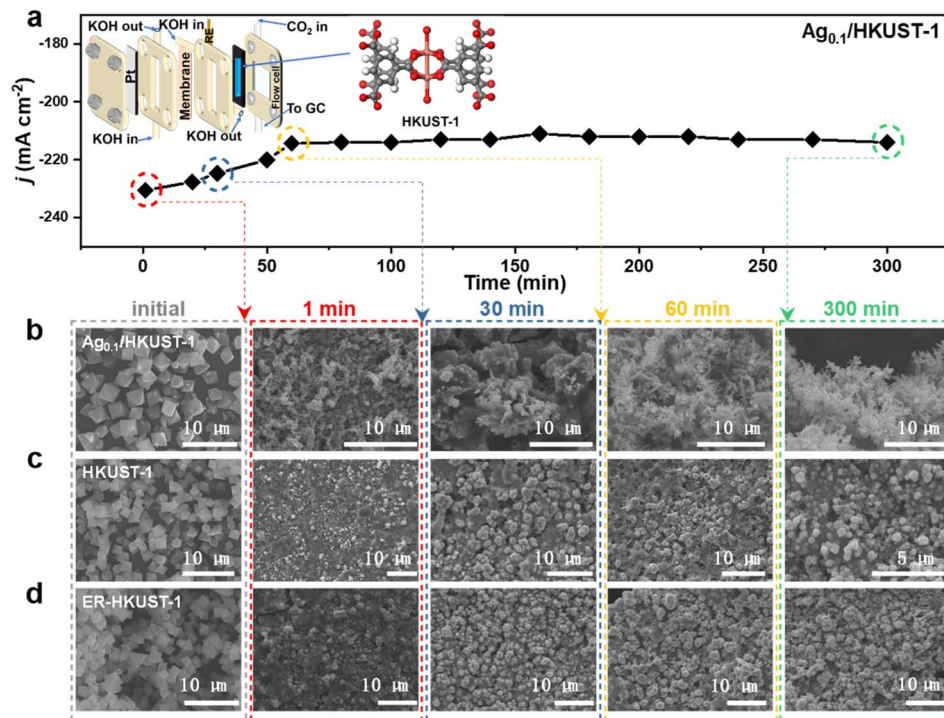


Fig. 2 (a) Chronoamperometry curve of  $\text{Ag}_{0.1}/\text{HKUST-1}$  during *in situ* electrochemical reconstruction at  $-1.3$  V vs. RHE, and SEM images of (b)  $\text{Ag}_{0.1}/\text{HKUST-1}$ , (c) HKUST-1 and (d) ER-HKUST-1 collected at 0, 1, 30, 60, and 300 min.

samples after 1 h and 5 h of electrolysis presented identical nanostructures, further confirming the rapid reconstruction finished within 1 h. Accordingly, the disappearance of the characteristic peaks of the benzene ring in FT-IR indicated that the organometallic framework has been drastically destroyed (Fig. S11, ESI†). This is distinct from the previous reports of ligand-retaining Cu surfaces (*e.g.*,  $\text{Cu}_2\text{O}@ \text{CuHHTP}$ ,<sup>17</sup>  $\text{Cu}_2(\text{HCOO})_3$  clusters,<sup>19</sup>  $\text{PPy}/\text{HKUST-1}$ ,<sup>21</sup> and  $\text{PANI}/\text{HKUST-1}$  (ref. 21)), and guarantees a reliable platform to unravel the structure–activity relationship of *in situ* formed interfaces.

The restructured electrocatalysts from HKUST-1, ER-HKUST-1 and  $\text{Ag}_{0.1}/\text{HKUST-1}$  after 1 h of  $\text{CO}_2\text{RR}$  were denoted as  $\text{Cu}_\text{H}$ -HKUST-1,  $\text{Cu}/\text{Cu}_2\text{O}_{\text{ER-HKUST-1}}$  and  $\text{Ag}/\text{Cu}/\text{Cu}_2\text{O}_{\text{Ag}_{0.1}/\text{HKUST-1}}$ , respectively. To minimize the impact of oxidation, the samples were immediately transferred to an argon-filled glovebox for further characterization. As depicted in their XRD patterns (Fig. 3a), the diffraction peaks of the original framework disappeared. Instead, typical peaks of  $\text{Cu}(111)$  and  $(200)$  were detected at  $2\theta = 43.3^\circ$  and  $50.4^\circ$ , respectively. Besides, the visible  $\text{Cu}_2\text{O}(111)$  and  $(200)$  in both  $\text{Cu}/\text{Cu}_2\text{O}_{\text{ER-HKUST-1}}$  and  $\text{Ag}/\text{Cu}/\text{Cu}_2\text{O}_{\text{Ag}_{0.1}/\text{HKUST-1}}$ , and the  $\text{Ag}(111)$  and  $(200)$  in  $\text{Ag}/\text{Cu}/\text{Cu}_2\text{O}_{\text{Ag}_{0.1}/\text{HKUST-1}}$  confirmed the co-presence of multiple phases, *i.e.*,  $\text{Cu}/\text{Cu}_2\text{O}$  and  $\text{Ag}/\text{Cu}/\text{Cu}_2\text{O}$ . In the Cu 2p XPS profiles (Fig. 3b), unlike the pre-catalysts, the peak of  $\text{Cu(II)}$  was absent in the reconstructed samples, and only the peak at 932.4 eV associated with  $\text{Cu(0)}/\text{Cu(I)}$  was observed, which indicated the reduction of  $\text{Cu(II)}$  at the applied potential.  $\text{Cu}/\text{Cu}_2\text{O}_{\text{ER-HKUST-1}}$  and  $\text{Ag}/\text{Cu}/\text{Cu}_2\text{O}_{\text{Ag}_{0.1}/\text{HKUST-1}}$  showed peaks at 914.3 and 917.3 eV in the AES, corresponding to  $\text{Cu(I)}$  and  $\text{Cu(0)}$  species,<sup>40</sup> while only

$\text{Cu(0)}$  was present on  $\text{Cu}_{\text{HKUST-1}}$  (Fig. 3c), which were consistent with the XRD results. Compared to the pre-catalysts, the peak of Ag 3d on  $\text{Ag}/\text{Cu}/\text{Cu}_2\text{O}_{\text{Ag}_{0.1}/\text{HKUST-1}}$  shifted toward a lower binding energy (Fig. S12, ESI†), probably due to Ag aggregation along with the electrochemical reconstruction.<sup>41</sup>

The high-resolution TEM (HR-TEM) image of  $\text{Ag}/\text{Cu}/\text{Cu}_2\text{O}_{\text{Ag}_{0.1}/\text{HKUST-1}}$  clearly showed the interfaces of  $\text{Ag}/\text{Cu}/\text{Cu}_2\text{O}$  (Fig. 3d). The lattice fringes of 0.181, 0.204 and 0.245 nm could be indexed to  $\text{Cu}(200)$ ,  $\text{Cu}(111)$  and  $\text{Cu}_2\text{O}(111)$ , respectively, and those of 0.204 and 0.235 nm were assigned to

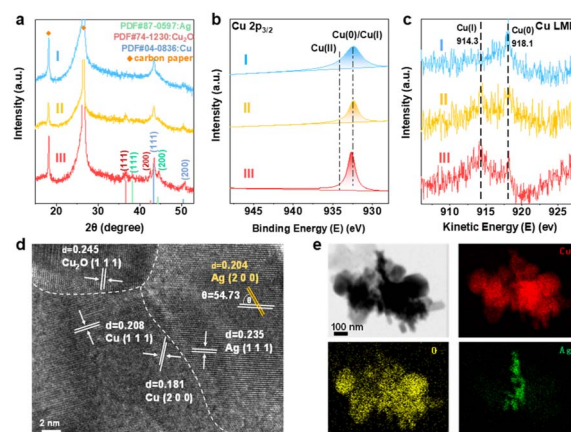


Fig. 3 (a) XRD patterns, (b) high-resolution Cu  $2p_{3/2}$  XPS and (c) Cu LMM AES of (I)  $\text{Cu}_{\text{HKUST-1}}$ , (II)  $\text{Cu}/\text{Cu}_2\text{O}_{\text{ER-HKUST-1}}$  and (III)  $\text{Ag}/\text{Cu}/\text{Cu}_2\text{O}_{\text{Ag}_{0.1}/\text{HKUST-1}}$ . (d) HR-TEM image and (e) elemental mapping of  $\text{Ag}/\text{Cu}/\text{Cu}_2\text{O}_{\text{Ag}_{0.1}/\text{HKUST-1}}$ .



Ag(200) and Ag(111). In comparison, the lattice planes of Cu(111) and Cu<sub>2</sub>O(111) were visible in Cu/Cu<sub>2</sub>O<sub>ER-HKUST-1</sub>, and only Cu(111) was observed in Cu<sub>HKUST-1</sub> (Fig. S13, ESI†). In Fig. 3e, the elements of Cu and O were uniformly distributed throughout the nanostructures, while the concentrated distribution of Ag suggested the formation of an Ag/Cu/Cu<sub>2</sub>O multiphase with abundant interfaces, rather than Ag-Cu alloys.

Furthermore, the X-ray absorption near edge structure (XANES) and extended X-ray absorption fine structure (EXAFS) of Ag/Cu/Cu<sub>2</sub>O<sub>Ag0.1HKUST-1</sub> were analysed to understand the local environments of Ag and Cu (Fig. S14, ESI†). The Ag K-edge overlapped with that of Ag foil, indicating a close-to-zero valence state of Ag in Ag/Cu/Cu<sub>2</sub>O<sub>Ag0.1HKUST-1</sub>. But the white line peak was slightly lower, consistent with the XPS data (Fig. S12, ESI†), which was probably due to the electron transfer from Cu to Ag. The electron transfer between Ag and Cu may lead to the formation of Ag-Cu bonds, as well as the existence of an Ag-Cu interface.<sup>42</sup> Accordingly, the Cu K-edge analysis presented a slightly higher valence state of Cu than that of the Cu<sub>2</sub>O reference. Moreover, the *k*<sup>2</sup>-weighted Ag K-edge EXAFS showed that the bond length and coordination number of Ag in Ag/Cu/Cu<sub>2</sub>O<sub>Ag0.1HKUST-1</sub> were slightly reduced, suggesting the formation of a heterostructure rather than alloys. Analogously, the increased Cu-O signal in the Cu K-edge EXAFS as compared with that of a Cu reference indicated the considerable amount of Cu<sub>2</sub>O in the restructured interfaces, and the lower Cu-O coordination number and the accordingly longer Cu-O bond in

comparison with those of a Cu<sub>2</sub>O reference might be due to the presence of heterogeneous interfaces. In addition, wavelet transform analysis highlighted the dominance of Ag-Ag and Cu-O bonds in the heterostructures, while Ag-O and Cu-Cu bonds are negligible, matching well with the EXAFS fitting results (Fig. S15 and Table S1, ESI†).

The electrochemical CO<sub>2</sub>RR performance of Cu<sub>HKUST-1</sub>, Cu/Cu<sub>2</sub>O<sub>ER-HKUST-1</sub> and Ag/Cu/Cu<sub>2</sub>O<sub>Ag0.1HKUST-1</sub> was evaluated in a flow cell with 1.0 M KOH as the electrolyte. The polarization curves showed the highest current densities of Ag/Cu/Cu<sub>2</sub>O<sub>Ag0.1HKUST-1</sub> among the three samples (Fig. 4a), indicative of the high activity of the restructured Ag/Cu/Cu<sub>2</sub>O. The electrolyte after reaction was analyzed by using <sup>1</sup>H nuclear magnetic resonance (NMR) spectroscopy, which suggested the negligible formation of liquid products (Fig. S16, ESI†). As evidenced by recent reports,<sup>38,43</sup> the higher coverage and transport efficiency of chemisorbed \*H derived from abundant H<sub>2</sub>O on gas-liquid-solid interfaces would benefit the generation of alcohols, the typical liquid products of the CO<sub>2</sub>RR. Herein, the superhydrophobic surface of the restructured Ag/Cu/Cu<sub>2</sub>O (Fig. S10, ESI†) probably prohibits the formation of alcohol products. With further regard to the same key step of \*CO coupling shared by ethylene and ethanol formation, we thereby focused on the gas products quantified by on-line GC for the understanding of the restructured interfaces, to avoid the superposition of instrumental errors (e.g., GC and NMR). Potentiostatic measurements at -1.0 to -1.5 V (vs. RHE) showed that Ag/Cu/

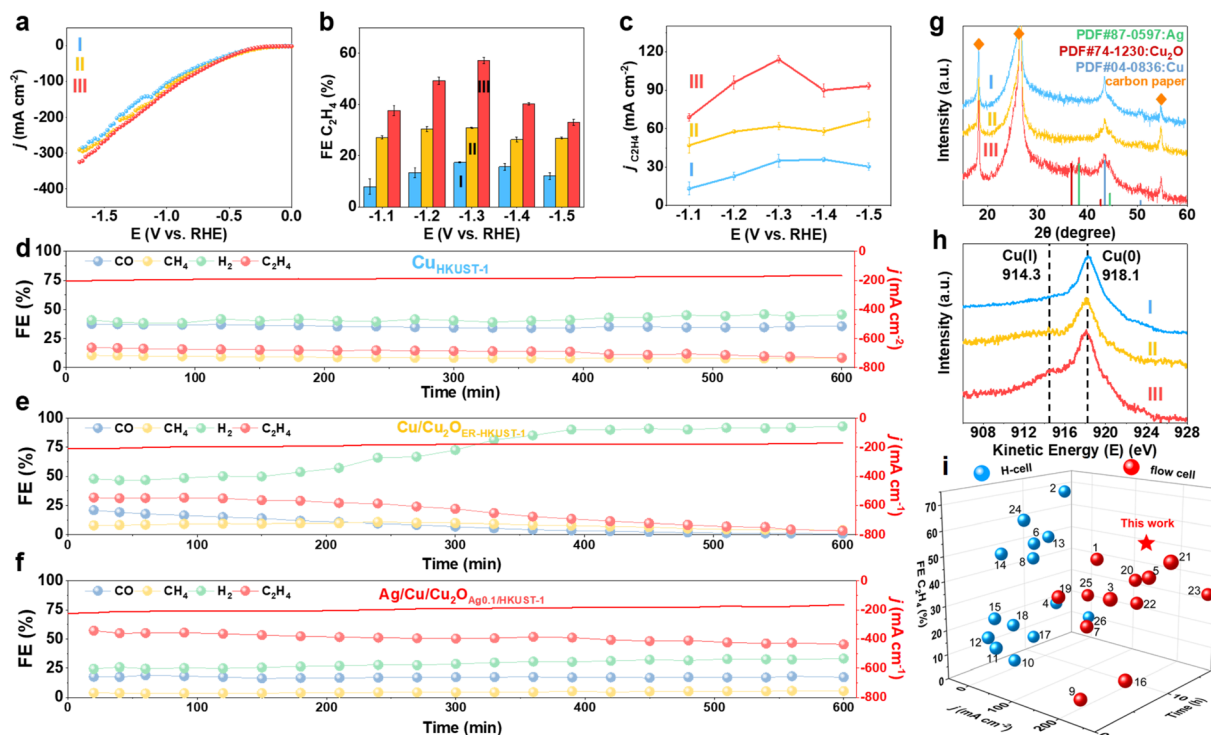


Fig. 4 (a) Polarization curves, (b) FE and (c) partial current density of C<sub>2</sub>H<sub>4</sub> at different applied potentials of (I) Cu<sub>HKUST-1</sub>, (II) Cu/Cu<sub>2</sub>O<sub>ER-HKUST-1</sub> and (III) Ag/Cu/Cu<sub>2</sub>O<sub>Ag0.1HKUST-1</sub> in CO<sub>2</sub>-saturated 1.0 M KOH. Chronoamperometric stability tests of (d) Cu<sub>HKUST-1</sub>, (e) Cu/Cu<sub>2</sub>O<sub>ER-HKUST-1</sub> and (f) Ag/Cu/Cu<sub>2</sub>O<sub>Ag0.1HKUST-1</sub>. (g) XRD patterns and (h) Cu LMM AES of Cu<sub>HKUST-1</sub>, Cu/Cu<sub>2</sub>O<sub>ER-HKUST-1</sub> and Ag/Cu/Cu<sub>2</sub>O<sub>Ag0.1HKUST-1</sub> after the CO<sub>2</sub>RR (600 min). (i) Performance of Ag/Cu/Cu<sub>2</sub>O<sub>Ag0.1HKUST-1</sub> compared with the recently reported Cu-based electrocatalysts (the numbers of reference samples are obtained from Table S2, ESI†).<sup>16,18–20,35,44–64</sup>

$\text{Cu}_2\text{O}_{\text{Ag}_{0.1}/\text{HKUST-1}}$  produced mainly  $\text{C}_2\text{H}_4$  with the maximum FE of 57.2% at  $-1.3$  V vs. RHE, while this value was only 17.4% on  $\text{Cu}_{\text{HKUST-1}}$  (Fig. 4b). The reaction profiles of  $\text{Cu}_{\text{HKUST-1}}$ ,  $\text{Cu}/\text{Cu}_2\text{O}_{\text{ER-HKUST-1}}$  and  $\text{Ag}/\text{Cu}/\text{Cu}_2\text{O}_{\text{Ag}_{0.1}/\text{HKUST-1}}$ , including product FEs and current densities, are depicted in Fig. S17, ESI†. Accordingly,  $\text{Ag}/\text{Cu}/\text{Cu}_2\text{O}_{\text{Ag}_{0.1}/\text{HKUST-1}}$  afforded a higher partial current density of  $\text{C}_2\text{H}_4$  ( $j_{\text{C}_2\text{H}_4}$ ) than  $\text{Cu}_{\text{HKUST-1}}$  and  $\text{Cu}_{\text{ER-HKUST-1}}$  (Fig. 4c), confirming the promoted ethylene production over  $\text{Ag}/\text{Cu}/\text{Cu}_2\text{O}$  heterostructures. For comparison, either the reference sample consisting of physically mixed Cu, Ag and  $\text{Cu}_2\text{O}$  nanoparticles or the electro-deposited one delivered a lower FE of  $\text{C}_2\text{H}_4$  than  $\text{Ag}/\text{Cu}/\text{Cu}_2\text{O}_{\text{Ag}_{0.1}/\text{HKUST-1}}$  under the same conditions (Fig. S18, ESI†), which highlighted the key contribution of MOF precursors to construct active  $\text{Ag}/\text{Cu}/\text{Cu}_2\text{O}$  multi-interfaces. To further unravel the effect of Ag, the  $\text{CO}_2\text{RR}$  performance of a series of  $\text{Ag}/\text{Cu}/\text{Cu}_2\text{O}$  derived from  $\text{Ag}_n/\text{HKUST-1}$  frameworks was measured (Fig. S19, ESI†). With the increase of Ag content, the FE of  $\text{C}_2\text{H}_4$  gradually increased and then tended to decrease, which indicated the benefited synergy of active components on the *in situ* generated  $\text{Ag}/\text{Cu}/\text{Cu}_2\text{O}$  interfaces with an optimal composition.

The electrochemically active surface area (ECSA) of the catalysts could be evaluated in terms of double-layer capacitance ( $C_{\text{dl}}$ , Fig. S20, ESI†), on the basis of their proportional correlation.  $\text{Ag}/\text{Cu}/\text{Cu}_2\text{O}_{\text{Ag}_{0.1}/\text{HKUST-1}}$  presented a  $C_{\text{dl}}$  value of  $3.24 \text{ mF cm}^{-2}$ , exceeding those of  $\text{Cu}_{\text{ER-HKUST-1}}$  ( $2.68 \text{ mF cm}^{-2}$ ) and  $\text{Cu}/\text{Cu}_2\text{O}_{\text{HKUST-1}}$  ( $2.04 \text{ mF cm}^{-2}$ ), which indicated enriched active-sites after restructuring  $\text{Ag}/\text{Cu}/\text{Cu}_2\text{O}$  multi-interfaces. Meanwhile, electrochemical impedance spectroscopy (EIS) pointed out the relatively smaller electron-transfer resistance ( $R_{\text{ct}}$ ) on  $\text{Ag}/\text{Cu}/\text{Cu}_2\text{O}_{\text{Ag}_{0.1}/\text{HKUST-1}}$  (Fig. S21, ESI†), in good accordance with its higher activity.

The long-term stability was evaluated by conducting a chronoamperometric test (Fig. 4d–f). On  $\text{Cu}_{\text{HKUST-1}}$ , the main products were  $\text{H}_2$  and CO with FEs of  $\sim 40\%$  and  $\sim 35\%$ , respectively, and the FE of  $\text{C}_2\text{H}_4$  was lower than 18%. Although the  $\text{C}_2\text{H}_4$  production was impressively enhanced on  $\text{Cu}_{\text{ER-HKUST-1}}$  (FE $_{\text{C}_2\text{H}_4} \sim 30\%$ ) during the initial reaction, it suffered from a drastic decrease to  $<20\%$  after 300 min, concomitant with the increase of  $\text{H}_2$  production. In sharp comparison,  $\text{Ag}/\text{Cu}/\text{Cu}_2\text{O}_{\text{Ag}_{0.1}/\text{HKUST-1}}$  manifested a remarkably stable FE of  $\text{C}_2\text{H}_4$  ( $\sim 50\%$ ) within 600 min, which should be ascribed to the Ag additives. In addition, compared to  $\text{Cu}_{\text{HKUST-1}}$ ,  $\text{Cu}/\text{Cu}_2\text{O}_{\text{ER-HKUST-1}}$  and  $\text{Ag}/\text{Cu}/\text{Cu}_2\text{O}_{\text{Ag}_{0.1}/\text{HKUST-1}}$  showed a significantly lower CO yield and higher  $\text{C}_2\text{H}_4$  yield during the initial reactions, which was accounted for by the effective consumption of  $^*\text{CO}$  to produce  $\text{C}_2\text{H}_4$ . Afterwards, the CO production suffered a continuous decrease on  $\text{Cu}/\text{Cu}_2\text{O}_{\text{ER-HKUST-1}}$ , whereas it was almost constant on  $\text{Ag}/\text{Cu}/\text{Cu}_2\text{O}_{\text{Ag}_{0.1}/\text{HKUST-1}}$ , suggesting a dynamic balance of  $^*\text{CO}$  formation and self-coupling on  $\text{Ag}/\text{Cu}/\text{Cu}_2\text{O}$  interfaces. In other words,  $^*\text{CO}$  generated on Ag sites might spill over onto the  $\text{Cu}/\text{Cu}_2\text{O}$  interface to increase the surface coverage of  $^*\text{CO}$ , thereby promoting C–C coupling toward  $\text{C}_2\text{H}_4$  and retaining the balance with CO formation and consumption.<sup>30,32</sup> Furthermore, we characterized the three catalysts after the long-term  $\text{CO}_2\text{RR}$  test. The spent  $\text{Ag}/\text{Cu}/\text{Cu}_2\text{O}_{\text{Ag}_{0.1}/\text{HKUST-1}}$  showed a well-retained phase composition ( $\text{Ag}/\text{Cu}/\text{Cu}_2\text{O}$ ) in XRD (Fig. 4g). The HR-TEM

images and the elemental mapping of  $\text{Ag}/\text{Cu}/\text{Cu}_2\text{O}_{\text{Ag}_{0.1}/\text{HKUST-1}}$  clearly presented the interfaces of  $\text{Ag}/\text{Cu}/\text{Cu}_2\text{O}$  (Fig. S22, ESI†), indicating the good structural stability. By contrast, the  $\text{Cu}_2\text{O}(111)$  and  $(200)$  disappeared on the used  $\text{Cu}/\text{Cu}_2\text{O}_{\text{ER-HKUST-1}}$ , consistent with the drastic decrease of  $\text{C}_2\text{H}_4$  FE. Accordingly, the AES results (Fig. 4h) identified the total disappearance of Cu(I) on  $\text{Cu}/\text{Cu}_2\text{O}_{\text{ER-HKUST-1}}$ , but the signal on  $\text{Ag}/\text{Cu}/\text{Cu}_2\text{O}_{\text{Ag}_{0.1}/\text{HKUST-1}}$  was still visible after the  $\text{CO}_2\text{RR}$ , which confirmed the promoted stability of Cu(I) assisted by Ag additives. There are two related thermodynamic factors taken into consideration. First, the substantial disparity in the formation enthalpies of  $\text{Cu}_2\text{O}$  ( $-169 \text{ kJ mol}^{-1}$ ) and  $\text{Ag}_2\text{O}$  ( $-31.1 \text{ kJ mol}^{-1}$ ) suggests that any Ag oxide resulting from oxygen exposure will be rapidly reduced by the adjacent Cu.<sup>32</sup> Second, Ag, with its higher redox potential relative to Cu, can accept electrons from Cu. In addition, the negligible change of the Ag 3d signal in XPS further underscored the durability of the  $\text{Ag}/\text{Cu}/\text{Cu}_2\text{O}$  ternary interfaces in  $\text{Ag}/\text{Cu}/\text{Cu}_2\text{O}_{\text{Ag}_{0.1}/\text{HKUST-1}}$  (Fig. S23, ESI†).

In further comparison with recently reported Cu-based electrocatalysts (Fig. 4i and Table S2, ESI†),  $\text{Ag}/\text{Cu}/\text{Cu}_2\text{O}_{\text{Ag}_{0.1}/\text{HKUST-1}}$  presented an outstanding overall performance with excellent  $\text{C}_2\text{H}_4$  FE, current output, and service life. Although some previous reports demonstrated the high FE of  $\text{C}_2\text{H}_4$ , they did not gain the high levels of current density and stability synchronously. For example,  $\text{CuPz}_2\text{-Act-30}$  exhibited a high  $\text{C}_2\text{H}_4$  FE of 67% in an H-cell, but the performance under high-current conditions such as in flow cells is still unclear.<sup>20</sup>  $\text{S-HKUST-1}$  displayed a  $\text{C}_2\text{H}_4$  FE of 57.2% at a current density of  $-400 \text{ mA cm}^{-2}$  in a flow cell, but the stability test (480 min) was only conducted at  $-150 \text{ mA cm}^{-2}$ .<sup>18</sup> Similarly,  $\text{Cu-PzH}$  yielded a  $\text{C}_2\text{H}_4$  FE of 60% at  $-1.0$  V (vs. RHE) with a large partial current density of  $346.46 \text{ mA cm}^{-2}$  while its stability remained for only 242 min.<sup>39</sup> More counterparts with rich Cu(I) species but prepared *via* other methods were further taken for comparison. For example,  $\text{Cu}_2\text{O-BN}$  and  $\text{Cu}_2\text{O}@/\text{SiO}_2\text{-NH}_2$  demonstrated stability exceeding 600 min,<sup>61,64</sup> whereas the  $\text{C}_2\text{H}_4$  FEs of 35% and 15% were deemed suboptimal. An AgCu single-atom alloy blended with Ag nanoparticles showed a  $94 \pm 4\%$  FE towards multi-carbon products at a high current density of  $\sim 720 \text{ mA cm}^{-2}$  in a flow cell, but the FE of  $\text{C}_2\text{H}_4$  was below 40%.<sup>42</sup> In contrast,  $\text{Ag}/\text{Cu}/\text{Cu}_2\text{O}_{\text{Ag}_{0.1}/\text{HKUST-1}}$  can achieve the superiority of  $\text{C}_2\text{H}_4$  FE ( $\sim 50\%$ ), current output ( $>180 \text{ mA cm}^{-2}$ ), and stability (600 min) at the same time, underscoring its promise for practical use. When a membrane electrode assembly (MEA) reactor is rationally designed for such restructured catalysts, we believe greater advances in performance, in particular the greater current density and long-term stability, can be accomplished.<sup>65</sup>

*In situ* Raman spectra were obtained and the  $\text{CO}_2\text{RR}$  test was performed to understand the dynamic changes of the restructured interfaces. Different from  $\text{Cu}_{\text{HKUST-1}}$ ,  $\text{Cu}/\text{Cu}_2\text{O}_{\text{ER-HKUST-1}}$  and  $\text{Ag}/\text{Cu}/\text{Cu}_2\text{O}_{\text{Ag}_{0.1}/\text{HKUST-1}}$  showed the band assigned to Cu(I) species at 520 and  $610 \text{ cm}^{-1}$  (Fig. 5a and b).<sup>37</sup> This band was well retained on  $\text{Ag}/\text{Cu}/\text{Cu}_2\text{O}_{\text{Ag}_{0.1}/\text{HKUST-1}}$  for 300 min, while it became weaker and disappeared on  $\text{Cu}/\text{Cu}_2\text{O}_{\text{ER-HKUST-1}}$ . In the meantime, this evolution was confirmed by the *in situ* Raman spectra collected at various potentials (Fig. S24, ESI†). Such *in situ* monitoring, highly consistent with the post- $\text{CO}_2\text{RR}$  AES analysis



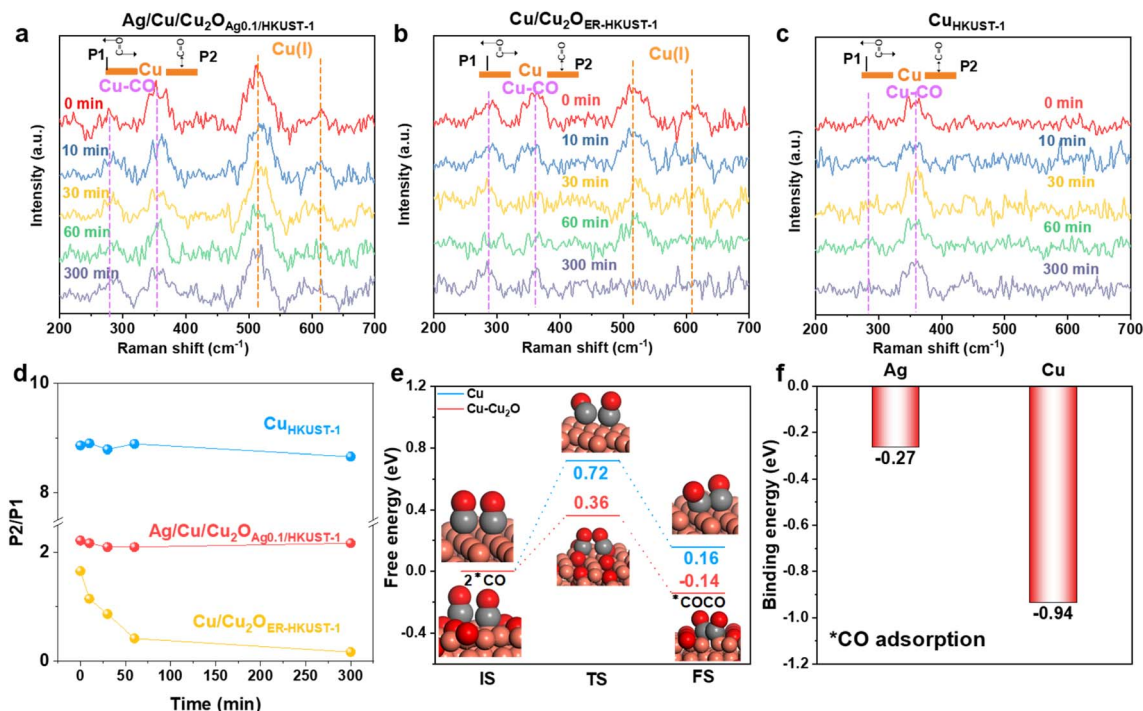


Fig. 5 *In situ* Raman spectra during the CO<sub>2</sub>RR under different reaction times of (a) Ag/Cu/Cu<sub>2</sub>O<sub>Ag0.1</sub>/HKUST-1, (b) Cu/Cu<sub>2</sub>O<sub>ER</sub>-HKUST-1 and (c) Cu<sub>HKUST-1</sub>, and (d) the corresponding evolution of P2/P1 ratios. (e) Energy profiles for the initial states (ISs), transition states (TSs) and final states (FSs) of \*CO-\*CO coupling on Cu and Cu-Cu<sub>2</sub>O models. (f) Energy profiles of \*CO adsorption on Ag and Cu.

(Fig. 4h), identified again the stabilization of the Cu(I) species by Ag. Furthermore, the peaks at 280 and 364.3 cm<sup>-1</sup>, corresponding to the restricted rotating (P1) and stretching (P2) models of adsorbed Cu-CO, respectively, could be detected on the surfaces, and the intensity ratio of P2/P1 peaks was a valid measure of the surface coverage of \*CO.<sup>36</sup> The P2 band was the main peak while the P1 was very weak on Cu<sub>HKUST-1</sub> (Fig. 5c and d), and their large ratio of 8.5–9.0 indicated the extremely high \*CO coverage on the Cu(0)-dominant surface,<sup>66</sup> consistent with the main distribution of CO in the products (Fig. 4d). In comparison with Cu/Cu<sub>2</sub>O<sub>ER</sub>-HKUST-1, Ag/Cu/Cu<sub>2</sub>O<sub>Ag0.1</sub>/HKUST-1 delivered a larger P2/P1 ratio associated with the higher \*CO coverage. More importantly, this ratio was kept at a high level above 2.0 on Ag/Cu/Cu<sub>2</sub>O<sub>Ag0.1</sub>/HKUST-1 during the CO<sub>2</sub>RR (0–300 min), but it drastically decreased on Cu/Cu<sub>2</sub>O<sub>ER</sub>-HKUST-1 (Fig. 5d). According to the recently evidenced tandem electrocatalysis on Ag/Cu interfaces,<sup>67,68</sup> we reasonably assumed that the CO spillover from Ag sites could increase the \*CO coverage on Cu(0)–Cu(I) ensembles, leading to the well-maintained P2/P1 ratio on Ag/Cu/Cu<sub>2</sub>O<sub>Ag0.1</sub>/HKUST-1 for the further C–C coupling.

To further understand the contribution of Ag and Cu<sub>2</sub>O on the C–C coupling and ethylene production, the model structures of Cu and Cu-Cu<sub>2</sub>O were taken for DFT calculations. As a critical step toward C<sub>2+</sub> products, the coupling of two \*CO was brought into focus. As shown in Fig. 5e, the kinetic barrier (0.36 eV) and enthalpy change (–0.14 eV) for the \*CO coupling on Cu-Cu<sub>2</sub>O are lower than those on Cu (0.72 and 0.16 eV), suggesting that the interfaces of Cu(0)–Cu(I) can effectively boost C<sub>2</sub> production. The coupling of two adjacent \*CO on Cu–Ag should

be difficult because of the high energy barrier (1.44 eV) (Fig. S25, ESI†), wherein the spillover of \*CO from Ag to Cu would be preferred. Numerous studies have found that Ag has a high selectivity for CO in the CO<sub>2</sub>RR which can provide adequate \*CO for the tandem catalysis toward C<sub>2</sub> products.<sup>30–32,67,68</sup> As indicated by the more negative \*CO binding energy on Cu (–0.94 eV) than that on Ag (–0.27 eV) (Fig. 5f), the spillover of the as-formed \*CO from Ag to Cu and even Cu(0)–Cu(I) interfaces is thermodynamically favorable. Therefore, a tandem mechanism is proposed, in which the CO produced by Ag sites can diffuse to the reactive interface of Cu–Cu<sub>2</sub>O with a low kinetic barrier for further coupling toward C<sub>2</sub>H<sub>4</sub>. In addition, Ag can stabilize the Cu(I) species to enable high ethylene production for a long time, which has been well validated by *in situ* Raman and *ex situ* XRD and AES.

Finally, we adopted other Cu-MOFs with the varied coordination as the pre-catalysts towards Ag/Cu/Cu<sub>2</sub>O interfaces, to examine the applicability of this strategy. With a similar Cu–O<sub>4</sub> structure but a layered crystalline structure, CuBDC (BDC = 1,4-benzenedicarboxylic acid) underwent extensive reconstruction from 2D crystals to smaller nanoparticles, which was beneficial for restructuring Ag/Cu/Cu<sub>2</sub>O interfaces when Ag was incorporated (Fig. S26, ESI†). Thanks to the rich interfaces of Ag/Cu/Cu<sub>2</sub>O, the reconstructed samples afforded the obviously higher FE of C<sub>2</sub>H<sub>4</sub> in comparison with that free from Ag. By contrast, CuPz<sub>2</sub> (Pz = pyrazol) with a Cu–N<sub>4</sub> structure cannot undergo the reconstruction under these working conditions due to the strong coordination of Cu–N<sub>4</sub> (Fig. S27, ESI†). When Ag was incorporated into CuPz<sub>2</sub>, the resulting



samples unfortunately increased the FE of CO, probably due to the preferred generation of CO on the loaded Ag nanoparticles. The accordingly reduced FE of C<sub>2</sub>H<sub>4</sub> also indicated the severely competitive reduction of CO<sub>2</sub> on Cu and Ag sites because of the absence of Ag/Cu interfaces. This is indirect proof for the tandem electrolysis towards C<sub>2</sub>H<sub>4</sub> over Ag/Cu/Cu<sub>2</sub>O<sub>Ag<sub>0.1</sub>/HKUST-1</sub> *via* \*CO spillover. It's clear that the coordination of Cu-based MOFs is important for restructuring Ag/Cu/Cu<sub>2</sub>O interfaces, although the ligands make negligible influences on the electrocatalytic performance indeed because they have already been removed during the reconstruction (Fig. S11, ESI†). The frangible Cu–O<sub>4</sub> nodes are the prerequisite for the reconstruction, while the strong Cu–N<sub>4</sub> requires more tough conditions (*e.g.*, more negative potentials) to drive the reconfiguration.<sup>20</sup>

## Conclusions

In summary, the directional *in situ* reconfiguration of Ag incorporating HKUST-1 frameworks was successfully introduced to restructure multi-phase Ag/Cu/Cu<sub>2</sub>O electrocatalysts highly active for the CO<sub>2</sub>RR. The reconstituted Ag/Cu/Cu<sub>2</sub>O exhibited outstanding performance for the selective electroreduction of CO<sub>2</sub> to C<sub>2</sub>H<sub>4</sub>, with superior FE, current output, and service life to the most of recently reported counterparts. The combination of *in/ex situ* characterizations (Raman, XRD, XPS and AES) and theoretical calculations demonstrated that Ag plays a crucial role in stabilizing Cu(I) and increasing CO surface coverage, while the resulting Cu/Cu<sub>2</sub>O interfaces significantly reduced the C–C coupling energy barrier toward the boosted ethylene production. This work not only offered a rational method to prepare highly active catalysts *via* electrochemical activation, but also deepened the understanding of the working state and mechanism on multi-phase interfaces. It's envisioned to gain further improvement *via* utilizing booming MOF pre-catalysts with more precise control over the coordination chemistry and dynamic evolution.

## Data availability

Data supporting the findings of this study are available within the article ESI.†

## Author contributions

Jiye Feng: synthesis, investigations, formal analysis, writing of the original draft, data curation. Wenbiao Zhang: DFT calculation, supervision. Danni Shi: experimental analysis, image polishing. Yingshuai Jia: proofreading of the original draft. Yi Tang: conceptualization, supervision, funding acquisition. Yuying Meng: conceptualization. Qingsheng Gao: conceptualization, supervision, writing – review and editing, funding acquisition.

## Conflicts of interest

There are no conflicts to declare.

## Acknowledgements

The authors appreciate the financial support from the National Natural Science Foundation of China (No. 22175077), Innovation Team Project in Guangdong Colleges and Universities (No. 2021KCXTD009), Guangdong Basic and Applied Basic Research Foundation (2023A1515240081), Guangzhou Science and Technology Program (No. 202201020071) and Fundamental Research Funds for the Central Universities (No. 21623103).

## Notes and references

- 1 P. De Luna, C. Hahn, D. Higgins, S. A. Jaffer, T. F. Jaramillo and E. H. Sargent, *Science*, 2020, **367**, eaav3506.
- 2 D. Gao, R. M. Aran-Ais, H. S. Jeon and B. Roldan Cuenya, *Nat. Catal.*, 2019, **2**, 198–210.
- 3 T. Yan, X. Chen, L. Kumari, *et al.*, *Chem. Rev.*, 2023, **123**, 10530–10583.
- 4 M. Kuang and G. Zheng, *Chem Catal.*, 2023, **3**, 100565.
- 5 Q. Chen, X. Wang, Y. Zhou, Y. Tan, H. Li, J. Fu and M. Liu, *Adv. Mater.*, 2024, **36**, 2303902.
- 6 S. Nitopi, E. Bertheussen, S. B. Scott, *et al.*, *Chem. Rev.*, 2019, **119**, 7610–7672.
- 7 M. G. Kibria, J. P. Edwards, C. M. Gabardo, D. Cao-Thang, A. Seifitokaldani, D. Sinton and E. H. Sargent, *Adv. Mater.*, 2019, **31**, 1807166.
- 8 B. Chang, H. Pang, F. Raziq, S. Wang, K.-W. Huang, J. Ye and H. Zhang, *Energy Environ. Sci.*, 2023, **16**, 4714–4758.
- 9 H. Yang, S. Li and Q. Xu, *Chin. J. Catal.*, 2023, **48**, 32–65.
- 10 R. M. Aran-Ais, F. Scholten, S. Kunze, R. Rizo and B. Roldan Cuenya, *Nat. Energy*, 2020, **5**, 317–325.
- 11 C. Xiao and J. Zhang, *ACS Nano*, 2021, **15**, 7975–8000.
- 12 Q. J. Wu, J. Liang, Y. B. Huang and R. Cao, *Acc. Chem. Res.*, 2022, **55**, 2978–2997.
- 13 H. L. Zhu, J. R. Huang, P. Q. Liao and X. M. Chen, *ACS Cent. Sci.*, 2022, **8**, 1506–1517.
- 14 X. Kang, Q. Zhu, X. Sun, J. Hu, J. Zhang, Z. Liu and B. Han, *Chem. Sci.*, 2016, **7**, 266–273.
- 15 D. Yao, C. Tang, A. Vasileff, X. Zhi, Y. Jiao and S.-Z. Qiao, *Angew. Chem., Int. Ed.*, 2021, **60**, 18178–18184.
- 16 X. Xie, X. Zhang, M. Xie, *et al.*, *Nat. Commun.*, 2022, **13**, 63.
- 17 J. D. Yi, R. Xie, Z. L. Xie, G. L. Chai, T. F. Liu, R. P. Chen, Y. B. Huang and R. Cao, *Angew. Chem., Int. Ed.*, 2020, **59**, 23641–23648.
- 18 C. F. Wen, M. Zhou, P. F. Liu, *et al.*, *Angew. Chem., Int. Ed.*, 2022, **61**, e202111700.
- 19 W. Zhang, C. Huang, J. Zhu, *et al.*, *Angew. Chem., Int. Ed.*, 2022, **61**, e202112116.
- 20 C. Liu, X.-D. Zhang, J.-M. Huang, M.-X. Guan, M. Xu and Z.-Y. Gu, *ACS Catal.*, 2022, **12**, 15230–15240.
- 21 J. Cheng, L. Chen, X. Xie, *et al.*, *Angew. Chem., Int. Ed.*, 2023, **62**, e202312113.
- 22 J.-X. Wu, S.-Z. Hou, X.-D. Zhang, M. Xu, H.-F. Yang, P.-S. Cao and Z.-Y. Gu, *Chem. Sci.*, 2019, **10**, 2199–2205.
- 23 J.-Y. Kim, D. Hong, J.-C. Lee, *et al.*, *Nat. Commun.*, 2021, **12**, 3765.



- 24 C. Hahn, T. Hatsukade, Y.-G. Kim, A. Vailionis, J. H. Baricuatro, D. C. Higgins, S. A. Nitopi, M. P. Soriaga and T. F. Jaramillo, *Proc. Natl. Acad. Sci. U. S. A.*, 2017, **114**, 5918–5923.
- 25 D. Wakerley, S. Lamaison, J. Wicks, *et al.*, *Nat. Energy*, 2022, **7**, 130–143.
- 26 X.-D. Zhang, T. Liu, C. Liu, *et al.*, *J. Am. Chem. Soc.*, 2023, **145**, 2195–2206.
- 27 S.-C. Lin, C.-C. Chang, S.-Y. Chiu, H.-T. Pai, T.-Y. Liao, C.-S. Hsu, W.-H. Chiang, M.-K. Tsai and H. M. Chen, *Nat. Commun.*, 2020, **11**, 3525.
- 28 W. Zhang, Y. Yang, Y. Tang and Q. Gao, *J. Energy Chem.*, 2022, **70**, 414–436.
- 29 C.-J. Chang, S.-C. Lin, H.-C. Chen, J. Wang, K. J. Zheng, Y. Zhu and H. M. Chen, *J. Am. Chem. Soc.*, 2020, **142**, 12119–12132.
- 30 C. Chen, Y. Li, S. Yu, S. Louisia, J. Jin, M. Li, M. B. Ross and P. Yang, *Joule*, 2020, **4**, 1688–1699.
- 31 T. Yang, M. Kuang and J. Yang, *Nano Res.*, 2023, **16**, 8670–8683.
- 32 T. T. H. Hoang, S. Verma, S. Ma, T. T. Fister, J. Timoshenko, A. I. Frenkel, P. J. A. Kenis and A. A. Gewirth, *J. Am. Chem. Soc.*, 2018, **140**, 5791–5797.
- 33 Z. Song, Y. Liu, Y. Zhong, Q. Guo, J. Zeng and Z. Geng, *Adv. Mater.*, 2022, **34**, 2204306.
- 34 H. Sun, X. Han, K. Liu, B. Shen, J. Liu, D. Wu and X. Shi, *Ind. Eng. Chem. Res.*, 2017, **56**, 9541–9550.
- 35 N. Dae-Hyun, O. S. Bushuyev, J. Li, *et al.*, *J. Am. Chem. Soc.*, 2018, **140**, 11378–11386.
- 36 C. Zhan, F. Dattila, C. Rettenmaier, A. Bergmann, S. Kuhl, R. Garcia-Muelas, N. Lopez and B. R. Cuenya, *ACS Catal.*, 2021, **11**, 7694–7701.
- 37 S. Mu, H. Lu, Q. Wu, L. Li, R. Zhao, C. Long and C. Cui, *Nat. Commun.*, 2022, **13**, 3694.
- 38 Y. Lin, T. Wang, L. Zhang, *et al.*, *Nat. Commun.*, 2023, **14**, 3575.
- 39 Y. Wu, J. Feng, D. Shi, W. Zhang, Y. Tang and Q. Gao, *Chem. Commun.*, 2023, **59**, 10428–10431.
- 40 Y. Guo, C. Feng, S. Wang, *et al.*, *J. Mater. Chem. A*, 2020, **8**, 24477–24485.
- 41 I. Lopez-Salido, D. C. Lim and Y. D. Kim, *Surf. Sci.*, 2005, **588**, 6–18.
- 42 C. Du, J. P. Mills, A. G. Yohannes, *et al.*, *Nat. Commun.*, 2023, **14**, 6142.
- 43 M. Luo, Z. Wang, Y. C. Li, *et al.*, *Nat. Commun.*, 2019, **10**, 5814.
- 44 Z. Weng, J. Jiang, Y. Wu, *et al.*, *J. Am. Chem. Soc.*, 2016, **138**, 8076–8079.
- 45 S. Kusama, T. Saito, H. Hashiba, A. Sakai and S. Yotsuhashi, *ACS Catal.*, 2017, **7**, 8382–8385.
- 46 Y.-S. Cheng, X.-P. Chu, M. Ling, N. Li, K.-L. Wu, F.-H. Wu, H. Li, G. Yuan and X.-W. Wei, *Catal. Sci. Technol.*, 2019, **9**, 5668–5675.
- 47 F. Yang, A. Chen, P. L. Deng, Y. Zhou, Z. Shahid, H. Liu and B. Y. Xia, *Chem. Sci.*, 2019, **10**, 7975–7981.
- 48 A. Guan, Z. Chen, Y. Quan, *et al.*, *ACS Energy Lett.*, 2020, **5**, 1044–1053.
- 49 J.-D. Yi, R. Xie, Z.-L. Xie, G.-L. Chai, T.-F. Liu, R.-P. Chen, Y.-B. Huang and R. Cao, *Angew. Chem., Int. Ed.*, 2020, **59**, 23641–23648.
- 50 Y. Zhou, S. Chen, S. Xi, Z. Wang, P. Deng, F. Yang, Y. Han, Y. Pang and B. Y. Xia, *Cell Rep. Phys. Sci.*, 2020, **1**, 100182.
- 51 H. Huo, J. Wang, Q. Fan, Y. Hu and J. Yang, *Adv. Energy Mater.*, 2021, **11**, 2102447.
- 52 X.-F. Qiu, H.-L. Zhu, J.-R. Huang, P.-Q. Liao and X.-M. Chen, *J. Am. Chem. Soc.*, 2021, **143**, 7242–7246.
- 53 L. Zhang, X.-X. Li, Z.-L. Lang, *et al.*, *J. Am. Chem. Soc.*, 2021, **143**, 3808–3816.
- 54 Y. Zhang, L.-Z. Dong, S. Li, X. Huang, J.-N. Chang, J.-H. Wang, J. Zhou, S.-L. Li and Y.-Q. Lan, *Nat. Commun.*, 2021, **12**, 6390.
- 55 R. Chen, L. Cheng, J. Liu, Y. Wang, W. Ge, C. Xiao, H. Jiang, Y. Li and C. Li, *Small*, 2022, **18**, 2200720.
- 56 D.-S. Huang, H.-L. Zhu, Z.-H. Zhao, J.-R. Huang, P.-Q. Liao and X.-M. Chen, *ACS Catal.*, 2022, **12**, 8444–8450.
- 57 L.-L. Zhuo, P. Chen, K. Zheng, *et al.*, *Angew. Chem., Int. Ed.*, 2022, **61**, e202204967.
- 58 B. Kim, Y. C. Tan, Y. Ryu, *et al.*, *ACS Energy Lett.*, 2023, **8**, 3356–3364.
- 59 R. Wang, J. Liu, Q. Huang, *et al.*, *Angew. Chem., Int. Ed.*, 2021, **60**, 19829–19835.
- 60 P. P. Guo, Z. H. He, S. Y. Yang, W. T. Wang, K. Wang, C. C. Li, Y. Y. Wei, Z. T. Liu and B. X. Han, *Green Chem.*, 2022, **24**, 1527–1533.
- 61 Y. Zhou, Y. Yao, R. Zhao, *et al.*, *Angew. Chem., Int. Ed.*, 2022, **134**, e202205832.
- 62 X. Ma, X. Song, L. Zhang, *et al.*, *Green Chem.*, 2023, **25**, 7635–7641.
- 63 F. Yu, X. Liu, L. Liao, G. Xia and H. Wang, *Small*, 2023, **19**, 2301558.
- 64 Z.-Y. Zhang, H. Tian, H. Jiao, X. Wang, L. Bian, Y. Liu, N. Khaorapapong, Y. Yamauchi and Z.-L. Wang, *J. Mater. Chem. A*, 2024, **12**, 1218–1232.
- 65 Y. Liang, J. Zhao, Y. Yang, *et al.*, *Nat. Commun.*, 2023, **14**, 474.
- 66 T.-C. Chou, C.-C. Chang, H.-L. Yu, *et al.*, *J. Am. Chem. Soc.*, 2020, **142**, 2857–2867.
- 67 J. Huang, M. Mensi, E. Oveisi, V. Mantella and R. Buonsanti, *J. Am. Chem. Soc.*, 2019, **141**, 2490–2499.
- 68 Y. Yu, D. Wang, Y. Hong, T. Zhang, C. Liu, J. Chen, G. Qin and S. Li, *Chem. Commun.*, 2022, **58**, 11163–11166.

